Unsupervised detection of vineyards by 3D point-cloud UAV photogrammetry for precision agriculture

Unsupervised detection of vineyards by 3D point-cloud UAV photogrammetry for precision agriculture

Abstract

An effective management of precision viticulture processes relies on robust crop monitoring procedures and, in the near future, to autonomous machine for automatic site-specific crop managing. In this context, the exact detection of vineyards from 3D point-cloud maps, generated from unmanned aerial vehicles (UAV) multispectral imagery, will play a crucial role, e.g. both for achieve enhanced remotely sensed data and to manage path and operation of unmanned vehicles.
In this paper, an innovative unsupervised algorithm for vineyard detection and vine-rows features evaluation, based on 3D point-cloud maps processing, is presented. The main results are the automatic detection of the vineyards and the local evaluation of vine rows orientation and of inter-rows spacing.
The overall point-cloud processing algorithm can be divided into three mains steps: (1) precise local terrain surface and height evaluation of each point of the cloud, (2) point-cloud scouting and scoring procedure on the basis of a new vineyard likelihood measure, and, finally, (3) detection of vineyard areas and local features evaluation.
The algorithm was found to be efficient and robust: reliable results were obtained even in the presence of dense inter-row grassing, many missing plants and steep terrain slopes. Performances of the algorithm were evaluated on vineyard maps at different phenological phase and growth stages. The effectiveness of the developed algorithm does not rely on the presence of rectilinear vine rows, being also able to detect vineyards with curvilinear vine row layouts.

Keywords: Precision viticulture; Remote sensing; UAV; 3D point-cloud modelling; Images processing

1. Introduction

Precision Agriculture (PA) is a modern farming concept, based on new technologies, tools and computer devices, aimed at improving and optimising agricultural production processes by monitoring crops and calibrating inputs and operations. The benefits come from quality and quantity increment of agricultural outputs and from reduction of the environmental impact, such as the waste of fertilisers, pesticides, fresh water and energy (Gimenez et al., 2015; Reina et al., 2017).
This approach is particularly significant in viticulture, where the adoption of modern techniques is required to guarantee high quality standards of wine production (Mania et al., 2015; Asproudi et al., 2016). Moreover, vinicultural areas are usually characterised by a disparate and irregular spatial distribution, steep terrains and large areas, resulting in difficult and expensive maintenance and inspection tasks for wine growers (Costa et al., 2016). In this context, modern PA techniques can help vine growers to define and monitor zones of different grape quality and productivity within the same vinicultural area (Hall et al., 2011; Torres-Sánchez et al., 2014), to adopt different farming practices according to grape variety (Arnó et al., 2011; Urretavizcaya et al., 2014), to prevent soil erosion (Rodrigo Comino et al., 2017) and to conserve organic soil matter.
An effective management of precision viticulture processes requires reliable crop monitoring procedure. Remote sensing represents a powerful technology for this task, providing huge amount of data, without any physical contact, from which valuable information can be derived, such as plant vigour level, radiometric indices, water stresses, grapevine size, missing plants (Khanal et al., 2017; Quebrajo et al., 2018). A proper management and organisation of data, based on Global Positioning Systems (GPS) and Geographical Information Systems (GIS), is required to make them effective in crop monitoring (Blauth and

Ducati, 2010), automatic guidance (Lipiński et al., 2016; García-Santillán et al., 2017) and for modern mobile devices (Stojanovic et al., 2017), also in GIS database system (Haase et al., 2016).
In agricultural remote sensing, multispectral satellite imagery has been widely studied and employed for crop monitoring and management (Arango et al., 2016). Recently, the deployment of unmanned aerial vehicles (UAVs) and modern light sensors (including hyperspectral, thermal and photogrammetric cameras), has led to relevant novelty in remote sensing technology (Zhang and Kovacs, 2012), providing cost-effective data for vineyard mapping with very high spatial resolution (< 10 cm·pixel-1) (Zarco-Tejada et al., 2013; MacDonald et al., 2016).
New dense data provided by UAV imagery has required the development of proper image processing and analysis techniques that, based on different mathematical approach (e.g. Gabor filtering, Fourier transform, etc.), have allowed to extract a set of vineyard information from aerial images. Investigated vineyard features are, e.g., vegetation indexes, pure vines pixel identification, wine row detection, inter-row width (Da Costa et al., 2007; Rabatel et al., 2008; Delenne et al., 2010; Comba et al., 2015).
Additional information regarding crops can be provided by recent three-dimensional (3D) point-cloud modelling. Point-cloud is a large dataset of points, referred to as a 3D coordinate system, representing spots of the external surface of visible objects, where light is reflected. Data for 3D crop modelling can be directly provided by laser scanner (such as light detection and ranging systems - LiDAR) (Mack et al., 2017) or derived from multispectral and thermal imagery (Herrero-Huerta et al., 2015) by photogrammetry and computer vision algorithms, such as Structure from Motion (SfM). Studies on data fusion from LiDAR and multispectral images can be found, aimed at improving the quality of the obtained models (Sankey et al., 2017).
The goodness of point-clouds modelling is strictly related to the registration process: although several commercial software are available, work is still ongoing to develop new methods for efficient keypoints detection in 3D point-cloud reconstruction (Shah et al., 2017). In addition to points spatial information, 3D models reconstructed from airborne imagery usually have also additional spectral information.
The importance of this new type of 3D models in monitoring and assessment tasks for biosciences is highlighted by valuable published researches: reliable algorithms to exploit 3D data in agricultural (Chang et al., 2017; Malambo et al., 2018), livestock (Mortensen et al., 2016; Guo et al., 2017) and food applications (Sture et al., 2016; Su et al., 2017) can be found.
In this work, an innovative unsupervised method for vineyards detection and features extraction from 3D point-cloud maps is presented. The proposed method allows to automatically generate map of land regions covered by vineyard and, in addition, provides information regarding local vine rows orientation and of inter-rows spacing, spatially organised in maps. In particular, the proposed method enhances the performances of existing algorithms based on two dimensional (2D) images (Da Costa et al., 2007; Rabatel et al., 2008; Delenne et al., 2010; Comba et al., 2015; Primicerio et al., 2015; Primicerio et al., 2017) in detecting vineyards. Indeed, not requiring rectilinear vine rows, the proposed method can be profitably applied to complex scenarios (e.g. several parcels with complex shapes, curvilinear vine rows, sloped areas, presence of other vegetation).
This paper is structured as follows: Section 2 reports information on the performed UAV acquisition campaign aimed at aerial images collection and subsequent point-cloud maps generation, together with georeferencing procedure details. Section 3 describes the developed unsupervised algorithm, organised into three main processing steps. The results obtained by processing four point-cloud maps are discussed in Section 4, while Section 5 reports conclusions and future developments.
Animations of several figures of the paper are available as supplementary materials (MX.mp4 video files) in the article electronic version, published online. These might be used by the interested reader in order to have a dynamic representation of the various processing phases.

2. Three-dimensional point-cloud maps

The effectiveness of the proposed unsupervised method for vineyard detection was evaluated by processing a set of four 3D point-cloud maps of a region located in Serralunga d'Alba (Piedmont, Northwest of Italy). The monitored area covers a surface of about 2.5 hectares, including three entire vineyard parcels and several partial ones, whose latitude and longitude positions in the World Geodetic System 1984 (WGS84) range between $[44.62334° \ 44.62539°]$ and $[7.99855° \ 8.00250°]$ respectively (Fig. 1). The region is characterised by a sloped land conformation, with an elevation ranging from 330 to 420 meters above sea level and a predominantly southwest orientation.

Each point-cloud map was generated with the Agisoft PhotoScan® software (Agisoft©, 2017), by processing a set of more than 1000 aerial images acquired with an airborne Parrot Sequoia® multispectral camera (Parrot© SA, 2017). Camera calibration procedure was performed before images alignment task and, in addition, a radiometric calibration was applied to the image blocks by using reference images of a Micasense calibrated reflectance panel acquired before and after each UAV flight. With a flight time of 15 minutes, the UAV path was planned to maintain its flight height at close to 35 meters with respect to the terrain by properly defining waypoint sets for each mission blocks on the base of the cropland GIS map. The planned UAV path is a set of rectilinear segments approximating the land height contour lines. To move from one to the next, short perpendicular movements were performed. The flight path was controlled by the drone guidance platform, and finally the log was checked after each flight. With this specification, the aerial images average ground sample distance (GSD) resulted in about $5 \ \mathrm{cm} \cdot \mathrm{pixel}^{-1}$, which allowed for a 3D point-cloud mean density of about 1450 units per m^2 of map surface.

A set of 12 ground markers was placed on selected vine trellis poles within the monitored area, well distinguishable in the UAV aerial images. The accurate markers position (10 cm accuracy), determined with a differential GPS, was used as Ground Control Points (GCP) during image blocks alignments to georeference the point-clouds in a geodetic coordinates frame.

The UAV flights were performed on four dates over the 2017 crop season to record different vines vegetative stages, which were: (1) one week before the flowering (May 15th), (2) 30 days after flowering (June 29th, presence of about 1 cm diameter green grapes), (3) 50% of the veraison (August 1st) and (4) 6 days before the harvesting (September 23rd). In particular, it should be noted that the meteorological course of the 2017 season showed anomalies related to the average temperature and rainfall trends of the region. Temperature values above the seasonal average in March led to an anticipation of the vine bud break by about 15 days. A sudden decrease in temperatures in the second half of April caused severe frost damage on plants in some vineyards and a more general slowing of the vine vegetative growing. The phases of flowering and of fruit set, partially influenced by this phenomenon, occurred with an advance of 10-15 days. The total rainfall of the season was much lower than the averages of recent years (480 mm in 2017 compared to an average of the last 12 years of about 800 mm), particularly during August and September, months in which the grape ripening is refined and completed. The reduced water availability for plants contributed in part to accelerating ripening and to determining an advance of about 10 days of veraison and of commercial harvest.

A point-cloud map is here formally defined as a set $S_1^{\{\mathrm{WGS84}\}}$ of points represented by array $p_\mathrm{i} = [\varphi_\mathrm{i}, \ \lambda_\mathrm{i}, \ e_\mathrm{i}]^\mathrm{T}$, with $\mathrm{i} = 1, \dots, \mathrm{card}\left(S_1^{\{\mathrm{WGS84}\}}\right)$, where φ_i, λ_i and e_i are the WGS84 latitude, longitude and elevation coordinates of point $\mathrm{p_i}$ respectively. In order to represent the models from WGS84 coordinates to a local metric Cartesian reference system (LRF), the position of point $p_\mathrm{i} \in S_1^{\{\mathrm{WGS84}\}}$ was firstly expressed

into a geocentric Cartesian coordinates frame (Earth-Centered Earth-Fixed - ECEF) by using operator $f(\cdot)$ (Cai et al., 2011), obtaining the set

$$S_1^{\{\mathrm{ECEF}\}} = \left\{ p_\mathrm{i}^{\{\mathrm{ECEF}\}} = [x_\mathrm{i}, y_\mathrm{i}, z_\mathrm{i}]^\mathrm{T} = f\left(p_\mathrm{i}^{\{\mathrm{WGS84}\}}\right), \forall\, p_\mathrm{i}^{\{\mathrm{WGS84}\}} \in S_1^{\{\mathrm{WGS84}\}} \right\}. \quad (1)$$

Each point $p_\mathrm{i}^{\{\mathrm{ECEF}\}} \in S_1^{\{\mathrm{ECEF}\}}$ was then referred to a local reference frame as

$$p_\mathrm{i}^{\{\mathrm{LRF}\}} = -R_{\mathrm{ECEF}}^{\mathrm{LRF}}\, O_{\mathrm{LRF}}^{\{\mathrm{ECEF}\}} + R_{\mathrm{ECEF}}^{\mathrm{LRF}}\, p_\mathrm{i}^{\{\mathrm{ECEF}\}} \quad (2)$$

where $R_{\mathrm{ECEF}}^{\mathrm{LRF}}$ is the rotation matrix from ECEF to LRF and $O_{\mathrm{LRF}}^{\{\mathrm{ECEF}\}}$ is the LRF origin, expressed in ECEF coordinates. The $O_{\mathrm{LRF}}^{\{\mathrm{ECEF}\}}$ position was chosen in the south-western and lowest point of the observed land region, which is, according to the WGS84 coordinates, $O_{\mathrm{LRF}}^{\{\mathrm{WGS84}\}} = [\varphi_0, \lambda_0, \mathrm{e}_0]^\mathrm{T}$, with $\varphi_0 = \min\left(\left\{\varphi_\mathrm{i} \colon [\varphi_\mathrm{i}, \lambda_\mathrm{i}, e_\mathrm{i}]^\mathrm{T} \in S_1^{\{\mathrm{WGS84}\}}\right\}\right)$, $\lambda_0 = \min\left(\left\{\lambda_\mathrm{i} \colon [\varphi_\mathrm{i}, \lambda_\mathrm{i}, e_\mathrm{i}]^\mathrm{T} \in S_1^{\{\mathrm{WGS84}\}}\right\}\right)$ and $e_0 = \min\left(\left\{e_\mathrm{i} \colon [\varphi_\mathrm{i}, \lambda_\mathrm{i}, e_\mathrm{i}]^\mathrm{T} \in S_1^{\{\mathrm{WGS84}\}}\right\}\right)$. With this definition, $O_{\mathrm{LRF}}^{\{\mathrm{ECEF}\}}$ could not belong to point-cloud map $S_1^{\{\mathrm{ECEF}\}}$. Rotation matrix $R_{\mathrm{ECEF}}^{\mathrm{LRF}}$ was defined to obtain the $x^{\{\mathrm{LRF}\}}$ and $y^{\{\mathrm{LRF}\}}$ local axes tangent in $O_{\mathrm{LRF}}^{\{\mathrm{WGS84}\}}$ to the WGS84 parallel and meridian, respectively. With the axis $x^{\{\mathrm{LRF}\}}$ oriented to the east and $y^{\{\mathrm{LRF}\}}$ to the north, axis $z^{\{\mathrm{LRF}\}}$ turns out to be in an opposite direction with respect to the hearth centre.

Concerning the point-cloud map used in the algorithm discussion, the local reference frame origin $O_{\mathrm{LRF}}^{\{\mathrm{WGS84}\}}$ turns out to be located in $[44.62368°, 7.99868°, 293.8\ \mathrm{m}]^\mathrm{T}$, and the numerical values of matrix $R_{\mathrm{ECEF}}^{\mathrm{LRF}}$ and array $O_{\mathrm{LRF}}^{\{\mathrm{ECEF}\}}$ are

$$R_{\mathrm{ECEF}}^{\mathrm{LRF}} = \begin{bmatrix} -0.1391 & 0.9903 & 0 \\ -0.6956 & -0.0978 & 0.7117 \\ 0.7048 & 0.0991 & 0.7025 \end{bmatrix} \quad (3)$$

and

$$O_{\mathrm{LRF}}^{\{\mathrm{ECEF}\}} = (-4.5030, -0.6328, -4.4579)^\mathrm{T} \cdot 10^6 \mathrm{m} \quad (4)$$

3. Point-cloud processing algorithm

The proposed algorithm can automatically detect areas occupied by vineyard parcels within a given point-cloud map, evaluating the local vine rows orientation and inter-row spacing. The overall point-cloud processing algorithm can be divided into three main processing steps: (1) accurate local terrain surface and height evaluation of each point of the cloud, (2) point-cloud scouting and scoring procedure on the basis of a new vineyard likelihood measure, and, finally, (3) detection of vineyard areas and local features evaluation. Each algorithm step is here presented and discussed with the aid of graphics obtained by processing the point-cloud map generated from data acquired on June 29th 2017.

3.1 Points local height evaluation

For easiness of reading, whenever not explicitly expressed in the superscript, the considered reference frame is hereinafter assumed to be the local LRF, with $S_1 = S_1^{\{\mathrm{LRF}\}}$. Considering a point-cloud $S_1 = \{\, p_\mathrm{i} = [x_\mathrm{i},\ y_\mathrm{i},\ z_\mathrm{i}]^\mathrm{T} \in \mathbb{R}^3;\ \mathrm{i} = 1, \ldots, \mathrm{card}(S_1)\,\}$, where x_i, y_i and z_i are the spatial coordinates of each point of the cloud map (Fig. 2 and M1.mp4 file), the output of the first step of the algorithm is a new set

$$S_2 = \{\, q = [x, y, h]^\mathrm{T} \in \mathbb{R}^3 \colon \forall\, p = [x, y, z]^\mathrm{T} \in\ S_1\} \quad (5)$$

with $\mathrm{card}(S_2) = \mathrm{card}(S_1)$ and where, given a point $p \in S_1$, h is its relative height with respect to the local terrain surface.

A good estimation of h is strictly influenced by the accuracy of the terrain modelling process, which was properly defined to manage point-cloud map also on sloped terrains. To this extent, the proposed recursive procedure considers several local subsets of neighbouring points belonging to the original set S_1. Reliability of the relative height evaluation of point $p \in S_1$ was improved by computing value h as the average of a sequence of several assessments, each one performed with a local subset $\mathcal{A}_{\mathrm{x,y}} \subset S_1$ located in a different position (Fig. 3 and M2.mp4 file). The subset of points $\mathcal{A}_{\mathrm{x,y}}$, defined as

$$\mathcal{A}_{\mathrm{x,y}} = \{p \in S_1 : \exists\, \ell \in \mathcal{L} \mid \|p - \ell\|_2 < r_{\mathcal{A}}\}, \tag{6}$$

is constituted by points p within a cylindrical volume with radius $r_{\mathcal{A}}$, centered in (x, y) and with vertical axis

$$\mathcal{L} = \{\ell \in \mathbb{R}^3 : \ell = a_{\mathcal{L}} \cdot s - b_{\mathcal{L}} \ \forall\, s \in \mathbb{R}\}, \tag{7}$$

where $a_{\mathcal{L}} = [0, 0, 1]^{\mathrm{T}}$ and $b_{\mathcal{L}} = [x, y, 0]^{\mathrm{T}}$. An example of subsets $\mathcal{A}_{\mathrm{x_a,y_a}}$, centered in $a = (90, 110)$, is highlighted by a red cylindrical volume in Fig. 2 (and M1.mp4 file), while its enlargement is represented in Fig. 3 (and M2.mp4 file).

Considering a radius $r_{\mathcal{A}} = 5$ m, the terrain surface within $\mathcal{A}_{\mathrm{x,y}}$ can be profitably modelled by plane

$$T_0 = \{\,[x, y, z]^{\mathrm{T}} \in \mathbb{R}^3 : a_0(x - \bar{x}_0) + b_0(y - \bar{y}_0) + c_0(z - \bar{z}_0) = 0\} \tag{8}$$

where $\bar{x}_0$, $\bar{y}_0$ and $\bar{z}_0$ are the centroid coordinates of $\mathcal{A}_{\mathrm{x,y}}$ and coefficients a_0, b_0 and c_0 are obtained by solving the following optimisation problem

$$\min_{a_0, b_0, c_0} \sum_{\mathrm{i}=1}^{\mathrm{card}(\mathcal{A}_{\mathrm{x,y}})} \frac{\left(a_0(x_{\mathrm{i}} - \bar{x}_0) + b_0(y_{\mathrm{i}} - \bar{y}_0) + c_0(z_{\mathrm{i}} - \bar{z}_0)\right)^2}{a_0^2 + b_0^2 + c_0^2} \tag{9}$$

Due to the high density of points representing terrain surface in the point-cloud map, plane T_0 is usually well aligned to the local terrain. However, the points of subset $\mathcal{A}_{\mathrm{x,y}}$ not representing the terrain might introduce a bias in the terrain modelling (Fig. 4 and M3.mp4 file). This undesired behaviour can be overcome by a recursive procedure, by finding the interpolating plane $T^{(\mathrm{j}+1)}$ of the updated subset

$$\mathcal{A}_{\mathrm{x,y}}^{(\mathrm{j}+1)} = \left\{p \in \mathcal{A}_{\mathrm{x,y}}^{(\mathrm{j})} : \left|z - z_{\mathrm{T}^{(\mathrm{j})}}\right| < t_{\sigma^2}\left(\mathcal{A}_{\mathrm{x,y}}^{(\mathrm{j})}\right)\right\} \tag{10}$$

obtained by discarding points p with coordinate z greater than $t_{\sigma^2}\left(\mathcal{A}_{\mathrm{x,y}}^{(\mathrm{j})}\right)$ with respect to plane $T^{(\mathrm{j})}$. Indeed,

$$z_{\mathrm{T}^{(\mathrm{j})}} = -c_{\mathrm{j}}^{-1}\left(a_{\mathrm{j}}(x - \bar{x}_{\mathrm{j}}) + b_{\mathrm{j}}(y - \bar{y}_{\mathrm{j}})\right) + \bar{z}_{\mathrm{j}} \tag{11}$$

is the elevation coordinate of plane $T^{(\mathrm{j})}$ in (x, y), $\left[\bar{x}_{\mathrm{j}}, \bar{y}_{\mathrm{j}}, \bar{z}_{\mathrm{j}}\right]^{\mathrm{T}}$ are the centroid coordinates of subset $\mathcal{A}_{\mathrm{x,y}}^{(\mathrm{j})}$ and coefficients a_{j}, b_{j} and c_{j} are derived from Eq. (9), for subset $\mathcal{A}_{\mathrm{x,y}}^{(\mathrm{j})}$.

With a function t_{σ^2} inversely proportional to the variance of coordinate z of all points $p \in \mathcal{A}_{\mathrm{x,y}}^{(\mathrm{j})}$, the recursive procedure converges and stops when $\left|\mathrm{card}\left(\mathcal{A}_{\mathrm{x,y}}^{(\mathrm{j}+1)}\right) - \mathrm{card}\left(\mathcal{A}_{\mathrm{x,y}}^{(\mathrm{j})}\right)\right| \leq t_{\mathcal{A}}$.

The final relative height $h_{\mathcal{A}_{\mathrm{x,y}}}$ of point $p \in \mathcal{A}_{\mathrm{x,y}}$ with respect to plane $T^{(\mathrm{n})}$ can be thus easily computed as

$$h_{\mathcal{A}_{\mathrm{x,y}}} = z + c_{\mathrm{n}}^{-1}\left(a_{\mathrm{n}}(x - \bar{x}_{\mathrm{n}}) + b_{\mathrm{n}}(y - \bar{y}_{\mathrm{n}})\right) - \bar{z}_{\mathrm{n}} \tag{12}$$

The evaluation of $h_{\mathcal{A}_{\mathrm{x,y}}}$ was repeated on a set of subsets $\mathcal{A}_{\mathrm{x_i,y_i}}$, covering the entire point-cloud map S_1. For this purpose, set G of the considered points $(x_{\mathrm{i}}, y_{\mathrm{i}})$, organised on a regular grid on the horizontal plane with step l_{G}, was defined as

$$G = \left\{\left(x_{\mathrm{i}}, y_{\mathrm{j}}\right) \in \mathbb{R}^2 \ \forall\, x_{\mathrm{i}} \in G_{\mathrm{x}},\ y_{\mathrm{i}} \in G_{\mathrm{y}}\right\} \tag{13}$$

where $G_x = \{x_1, x_1 + l_G, \dots, x_2\}$ and $G_y = \{y_1, y_1 + l_G, \dots, y_2\}$, with $x_1 = \min\left(\{x_i : [x_i, y, z_i]^T \in S_1\}\right)$, $x_2 = \max\left(\{x_i : [x_i, y, z_i]^T \in S_1\}\right)$, $y_1 = \min\left(\{y_i : [x_i, y, z_i]^T \in S_1\}\right)$ and $y_2 = \max\left(\{y_i : [x_i, y, z_i]^T \in S_1\}\right)$. The procedure (Eqs. 6-12) was performed when $\mathrm{card}\left(\mathcal{A}_{x,y}\right) > t_\rho$, neglecting subset $\mathcal{A}_{x,y} = \emptyset$, to limit boundaries effects. Threshold t_ρ was set equal to $\rho_{S_1} \cdot \pi\, r_{\mathcal{A}}^2$, where ρ_{S_1} is the mean point-cloud density, defined as the number of points per m^2 of the xy-plane. Since the height $h_{\mathcal{A}_{x,y}}$ of a point $p \in S_1$ is usually evaluated several times, one for each subset $\mathcal{A}_{x,y} \supset p$, the final value of h is the average of all the performed evaluations. The obtained set of points S_2 is represented in Fig. 5 and M4.mp4 file.

3.2 Vineyard likelihood measure

Detection of point-cloud regions representing vineyards was achieved by introducing a likelihood scoring procedure, based on the analysis of the specific spatial distribution of model points. This process, analogously to the one described in § 3.1, requires the selection of a local point-cloud subset. A new cylindrical subset $\mathcal{B}_{x,y} \subset S_2$ with the vertical axis located in (x, y) and radius $r_\mathcal{B}$ was defined according to Eqs. 6 and 7. Examples of two subsets $\mathcal{B}_{x_b,y_b}$ and $\mathcal{B}_{x_c,y_c}$ of S_2, centered in $b = (200, 130)$ and $c = (230, 140)$ respectively, are highlighted with a cylinder in Fig. 5 (and M4.mp4 file), while their enlargements are represented in Figs. 6a and 6b.

The identification of vineyard areas within $\mathcal{B}_{x,y}$ was performed by looking at the set of all the relative distances between the points contained in $\mathcal{B}_{x,y}$. Indeed, point-cloud maps of vineyard areas have a peculiar regularity in the points spatial distribution. For this task, a new subset $\mathcal{B}'_{x,y}(\vartheta) \subset \mathcal{B}_{x,y}$ was introduced, defined as

$$\mathcal{B}'_{x,y}(\vartheta) = \left\{q \in \mathcal{B}_{x,y} : \exists\, u \in \mathcal{P}(\vartheta) \mid \|q - u\|_2 < t_\mathcal{B}\right\} \tag{14}$$

where

$$\mathcal{P}(\vartheta) = \left\{u = \left[u_x, u_y, u_z\right]^T \in \mathbb{R}^3 : \tan(\vartheta)\, u_x - u_y + (y_i - \tan(\vartheta)\, x_i) = 0\right\} \tag{15}$$

is a vertical plane passing through (x_i, y_i), which forms a counter-clockwise ϑ angle with the x-axis. In the two examples of Figs. 6a and 6b, the points contained in subsets $\mathcal{B}'_{x_b,y_b}(\vartheta)$ and $\mathcal{B}'_{x_c,y_c}(\vartheta)$, with $\vartheta = \frac{\pi}{2}$, are marked with red color, while their projections on plane $\mathcal{P}\left(\frac{\pi}{2}\right)$ are shown in Figs. 6c and 6d. Periodicity in the set of all the between-points distances

$$\mathcal{D}\left(\mathcal{B}'_{x,y}(\vartheta)\right) = \left\{d = \left\|q_i - q_j\right\|_2, \forall q_i, q_j \in \mathcal{B}'_{x,y}(\vartheta), 1 \le i, j \le \mathrm{card}\left(\mathcal{B}'_{x,y}(\vartheta)\right), i \ne j\right\} \tag{16}$$

was investigated by computing the normalised frequencies distribution histogram

$$H(\mathcal{D}(\cdot), s) = \mathrm{card}\{d \in \mathcal{D}(\cdot) : \ |d - s| < w\,\} \cdot \mathrm{card}\left(\mathcal{D}(\cdot)\right)^{-1} \tag{17}$$

where $s \in W_1 = \{0, \Delta s, 2\Delta s, \dots, d_{\max}\}$, W_1 is the set of all the histogram bins, Δs is the bin width and $d_{\max}$ is the upper limit of the considered distances d. For the sample subsets $\mathcal{B}_{x_b,y_b}$ and $\mathcal{B}_{x_c,y_c}$, the normalised frequencies distribution histograms $H(\mathcal{D}(\cdot), s)$ of $\mathcal{D}\left(\mathcal{B}'_{x_b,y_b}\left(\frac{\pi}{2}\right)\right)$ and of $\mathcal{D}\left(\mathcal{B}'_{x_c,y_c}\left(\frac{\pi}{2}\right)\right)$, computed with $d_{\max} = 10$ and $w = 0.1$ m, are shown in Figs. 6e and 6f respectively. A periodic trend can be noted in Fig. 6e.

Periodicity in distribution $H(\mathcal{D}(\cdot), s)$ was identified by means of the autocorrelation operator

$$R_{HH}(v) = \sum_{v=1}^{\mathrm{card}\, W_2} H(\mathcal{D}(\cdot), s) \cdot H(\mathcal{D}(\cdot), s - v) \tag{18}$$

with $W_2 = \{-d_{\max}, -d_{\max} + \Delta s, \dots, 0, \Delta s, \dots, d_{\max}\}$. The occurrence of a significant spatial regularity of points $q \in \mathcal{B}'_{\mathrm{x,y}}$, and thus the presence of a marked periodicity in $H(\mathcal{D}(\cdot), s)$, was proven by the existence of $n_{\hat{v}} > 3$ local maxima of $R_{\mathrm{HH}}(v)$, respectively located in $\hat{v}_{\mathrm{i}}$, with $i = 1, \dots, n_{\hat{v}}$. In addition, the period $I_{\mathrm{x,y}}(\vartheta)$ of $H(\mathcal{D}(\cdot), s)$, being related to the distances between two local maxima, can be evaluated as

$$I_{\mathrm{x,y}}(\vartheta) = \frac{\sum_{\mathrm{i}=1}^{n_{\hat{v}}-1} |\hat{v}_{\mathrm{i}+1} - \hat{v}_{\mathrm{i}}|}{n_{\hat{v}} - 1} \tag{19}$$

The autocorrelations $R_{\mathrm{HH}}(v)$ of both $H\left(\mathcal{D}\left(\mathcal{B}'_{\mathrm{x_b,y_b}}\left(\frac{\pi}{2}\right)\right), s\right)$ and $H\left(\mathcal{D}\left(\mathcal{B}'_{\mathrm{x_c,y_c}}\left(\frac{\pi}{2}\right)\right), s\right)$ are represented in Figs. 6g and 6h, together with the detected local maxima. The presence of a unique local maxima of $R_{\mathrm{HH}}(v)$ proves the absence of periodicity in the function.

However, an exhaustive and reliable analysis of subset $\mathcal{B}_{\mathrm{x,y}}$ requires an investigation of the possible regularity in points distribution along multiple directions ϑ_{i}, with $\vartheta_{\mathrm{i}} \in \Theta = \{\vartheta_{\min}, \vartheta_{\min} + \Delta_\vartheta, \dots, \vartheta_{\max}\}$ and $\vartheta_{\max} - \vartheta_{\min} \geq \pi$ radiant. Indeed, considering a subset $\mathcal{B}_{\mathrm{x,y}}$ representing a vineyard area, a plane $\mathcal{P}(\vartheta)$ aligned with vine row direction ϑ_v leads to a subset $\mathcal{B}'_{\mathrm{x,y}}(\vartheta)$ which intercepts one vine row at the most. In this case, periodicity and period $I_{\mathrm{x,y}}(\vartheta_v)$ cannot be determined. On the contrary, if $\mathcal{B}'_{\mathrm{x,y}}(\vartheta)$ intersects two or more vine rows, periodicity in $\mathcal{D}\left(\mathcal{B}'_{\mathrm{x,y}}(\vartheta)\right)$ and period $I_{\mathrm{x,y}}(\vartheta)$ can be found (Fig. 6f). Please note that $I_{\mathrm{x,y}}(\vartheta)$ has a minimum in $\vartheta_{\perp v} \cong \vartheta_v \pm \frac{\pi}{2}$, when subset $\mathcal{B}'_{\mathrm{x,y}}(\vartheta_{\perp v})$ is selected by considering a plane $\mathcal{P}(\vartheta_{\perp v})$ perpendicular to the local vine row direction. Set $\mathbb{I}_{\mathrm{x,y}}$ can thus be defined as $\mathbb{I}_{\mathrm{x,y}} = \{I_{\mathrm{x,y}}(\vartheta) \ \forall \ \vartheta \in \Theta\}$. A graphical representation of $\mathbb{I}_{\mathrm{x_b,y_b}}$ is shown in Fig. 7, where $I_{\mathrm{x_b,y_b}}(\vartheta)$ was computed with $\vartheta_{\min} = -\frac{5}{9}\pi$, $\vartheta_{\max} = \frac{5}{9}\pi$ and $\Delta_\vartheta = \frac{\pi}{18}$. Considering a subset $\mathcal{B}_{\mathrm{x,y}}$ not representing a vineyard area, no periodicity was usually found in $\mathcal{D}\left(\mathcal{B}'_{\mathrm{x,y}}(\vartheta)\right)$, with the exception of casual occurrences, easily detectible by introducing a scoring procedure of subset $\mathcal{B}_{\mathrm{x,y}}$.

The classification of subset $\mathcal{B}_{\mathrm{x,y}}$ representing vineyards was performed by introducing index $m(x, y)$, defined as

$$m(x, y) = \mathrm{card}\{I_{\mathrm{x,y}}(\vartheta) \in \mathbb{I}_{\mathrm{x,y}} : I_{\mathrm{x,y}}(\vartheta) < d_{\max}\} \cdot \mathrm{card}(\Theta)^{-1}. \tag{20}$$

Subsets $\mathcal{B}_{\mathrm{x,y}}$ not representing vineyards usually have values $m(x, y)$ which are lower than those selected from vineyard areas, therefore $m(x, y)$ can be considered as a robust local vineyard likelihood score.

3.3 Vineyard detection and features evaluation

The scouting procedure described in § 3.2 was performed on subsets $\mathcal{B}_{\mathrm{x_i,y_i}}$, with $(x_{\mathrm{i}}, y_{\mathrm{i}}) \in G$, covering the entire point-cloud map S_2. In this phase, grid step l_{G} was considered equal to 0.5 meters, which is a trade-off between high spatial resolution of results and limited computing time.

The results for the whole scoring procedure $M(S_2)$, where

$$M(S_2) = \{m(x, y) \ \forall \ (x, y) \in G\} \tag{21}$$

has a bimodal distribution, which allows for the application of a simple thresholding procedure on values $m(x, y)$ to reliably classify a subset $\mathcal{B}_{\mathrm{x,y}}$ as representing vineyards or not. The optimal threshold value was found to be $t_{\mathrm{m}} = 0.3$. Considering score set $M(S_2)$ as an organized matrix of values $m(x, y)$, a graphical representation of $M(S_2)$ is shown in Fig. 8, which was obtained by processing the June 2017 point-cloud map. By applying a simple sequence of morphological operations on binary map $M(S_2) > t_{\mathrm{m}}$ to remove noise, the map of the detected vineyard can finally be obtained (Fig. 9).

Additional information regarding local features of detected vineyards is also provided by the developed algorithm. Indeed, by analysing the trend of the entire set of $I_{\mathrm{x,y}}(\vartheta) \in \mathbb{I}_{\mathrm{x,y}}$, the local vine row direction $\vartheta_v(x,y)$ and inter-row spacing $d(x,y)$ can be evaluated. This task is performed by interpolating set $\mathbb{I}_{\mathrm{x,y}}$ with a second order polynomial function $f_p(\vartheta)$ to find direction $\vartheta_{\perp v}$ so that $f_p(\vartheta_{\perp v}) = \min\big(f_p(\vartheta)\big)$. Please note that, usually, $\vartheta_{\perp v} \notin \Theta$. The knowledge of direction $\vartheta_{\perp v}$, which is perpendicular to local vine row direction ϑ_v, allows the local inter-row spacing in (x,y) to be evaluated, by considering $\mathcal{B}'_{\mathrm{x,y}}(\vartheta_{\perp v})$. Indeed, the period $I_{\mathrm{x,y}}(\vartheta)$ of $H(\mathcal{D}(\cdot), s)$, when direction ϑ is perpendicular to vine row direction ϑ_v, is a good estimator of the inter-row spacing $d(x,y)$ in $\mathcal{B}_{\mathrm{x,y}}$ ($d_v(x,y) \cong I_{\mathrm{x,y}}(\vartheta_{\perp v})$). Graphical representations of $\vartheta_v(x,y)$ and $d_v(x,y)$ values, with $(x,y) \in G$ and properly organised in maps, are shown in Figs. 10a and 10b.

4. Results and discussion

The developed algorithm was implemented in Matlab® environment (Mathworks ®, 2018) and tested on four point-cloud maps, representing a land region extended on a steep terrain surface, covered with several vineyard plots (Nebbiolo and Moscato vine varieties), service paths, other vegetation and grass. The area (Serralunga d'Alba, Piedmont) was mapped on four different dates during 2017 to represent vineyards at different phenological phases. Since vine rows usually follow a curvilinear path aligned with land height contour lines, vineyard plots in the maps have irregular shapes due to the peculiar land slope.
As a validation of the presented vineyard detection algorithm, the plots boundaries within the considered test cropland were manually detected, defined by polygons in an open source geographic information system (QGIS, 2018) and exported as shapefile. After being imported in Matlab environment (Mathworks ®, 2018), the reference dataset was converted in a matrix with raster resolution compatible with the output of the automatic algorithm (in this work, 0.5 meters).
The accuracy of the vineyard detection process was thus evaluated according to five different indexes as: (1) Good detection, which considers the overlapping areas of automatically and manually detected vineyards; Over-detection (2) and Under-detection (3), considering vineyard areas automatically obtained by the proposed method which are larger or smaller than the manually detected one, respectively; Extra detection (4) and Missed detection (5) to assess the occurrence of regions completely wrongly classified by the algorithm as vineyard or not. All the defined indexes, summarised in Table 1, were defined as the percentage of the specific surface areas automatically obtained by the proposed method and the overall manually detected vineyard surface.
Maps of the detected vineyard areas, both automatic and manual, together with the spatial location of classification inaccuracies, are shown in Fig. 9, where regions properly classified as vineyards and over, under, extra and miss-detected areas are represented with different colours. The values of algorithm performance indexes on each single point-cloud map processing, together with the overall mean results, are detailed in Table 2. The results, with parameter values l_{G} defined in section § 3.2, have a spatial resolution of 0.5 meters. Since the point-cloud processing algorithm is affected by the border effect, where point-cloud subsets $\mathcal{B}_{\mathrm{x,y}}$ are partially out of the cloud, a region with a width equal to parameter $r_{\mathcal{B}}$ along the border was not considered in the results discussion.
The good detection index was found to be always greater than 90.0%, with an overall average value on the four point-cloud maps of 94.02%. The percentage of undesired misclassifications is very limited, with mean indexes of extra detection and missed detection equal to 0.64% and 0.01% respectively. Extra detection mainly occurs along point-cloud borders where 3D map reconstruction quality is lower. Missed-detection

can be considered null in all the processed point-cloud maps. It can be noted that over detection errors occur in case of small service paths parallel to the vine rows, with a width comparable to vineyard inter-row spacing. This undesired effect is absent if the path width differs by more than $\pm 10\%$ with respect to local inter-row spacing. The over detection index was found to be always lower than 4% with and average value over the four maps equal to 3.08%. The under-detection index is mainly due to the presence of a new parcel, with vines planted in the 2017 spring season, highlighted by a red line in Fig. 9b. Indeed, the under-detection index has high values, 7.52% and 7.67%, in the June and August point-cloud maps (Figs. 9a and 9b), when transplanted vine plants vigour was extremely low, while the misclassification decreases drastically (4.33%) in the September point-cloud processing. The algorithm thus proves to be very robust to plant vigour level, obtaining effective results with crops which have been implanted since less than one year.

The results on the additional information of the detected vineyards, regarding local inter-row spacing and vine row direction, are presented and discussed for the point-cloud map of July 29th 2017. From the graphical representations of vine row directions (Fig. 10a), it can be noted how small parcels, which have predominantly rectilinear vine rows, are characterised by uniform vine rows direction. On the contrary, larger ones, following the hilly land conformation, show a wider set of values $\vartheta_v(x, y)$, which translate in a non-uniform coloured region in Fig. 10a. Vine row spacing $d_v(x, y)$ in the whole detected vineyard within the monitored land region (Fig. 10b) results to be constant, with a value close to 2.6 meters (vineyard tractor size).

5. Conclusions

In this paper, an unsupervised algorithm that automatically detects vineyards within 3D point-cloud maps is presented. The algorithm is able to process a point-cloud map without any intervention or feedback from the user and requires a very limited number of parameters for its calibration. The effectiveness of the developed algorithm has been shown on the four point-cloud maps of a heterogeneous land region, with several irregularly shaped vine plots and other vegetation, acquired at different phenological phases. In addition, information on local vine row orientations and local inter-row distances, organized in proper georeferenced maps, are also provided by the algorithm.

The algorithm was found to be robust, providing reliable results in the case of vineyards with high plant failure rates, several vines growth, dense inter-row grassing and steep terrain slope, showing a low failure rate. A relevant additional strength of the developed methodology is the ability to process and detect vineyards not only with rectilinear vine rows, but also with curvilinear distributions, making the algorithm adaptable to a wide range of applications.

The possibility of automatically detecting vineyards within a point-cloud map may open the way to a new generation of unsupervised point-cloud processing algorithms aimed at evaluating crop status (such as vigour, leaf area index or fruit ripening) with detailed temporal and spatial resolutions, even at single plant level. Moreover, the information provided by the algorithm could also be used as input for the autonomous guidance of small vehicles, e.g. allowing automatic path planning along inter-row space.

Table 1. Results evaluation criteria of vineyard detection.

Case	Meaning
1. *Good detection*	correct detection of the vineyard region, matching manual evaluation
2. *Over-detection*	boundaries of automatically detected vineyard greater than real one
3. *Under-detection*	boundaries of automatically detected vineyard smaller than real one
4. *Extra detection*	non-vineyard region wrongly classified as vineyard
5. *Missed detection*	parcels totally not detected

Table 2. Results of vineyard detection (expressed as percentage of vineyard areas with respect to the overall manually detected vineyard surface) applied to four point-cloud maps. Overall mean performances of the developed point-cloud processing settlement are reported in the fifth column.

	Point-cloud May 15th 2017	**Point-cloud June 29th 2017**	**Point-cloud August 1st 2017**	**Point-cloud September 23rd 2017**	**Mean**
1. *Good detection*	95.62%	92.47%	92.33%	95.67%	94.02%
2. *Over-detection*	3.24%	2.93%	2.34%	3.79%	3.08%
3. *Under-detection*	4.38%	7.52%	7.67%	4.33%	5.98%
4. *Extra detection*	0.31%	0.97%	0.25%	1.04%	0.64%
5. *Missed detection*	0.02%	0.01%	0.01%	0.01%	0.01%

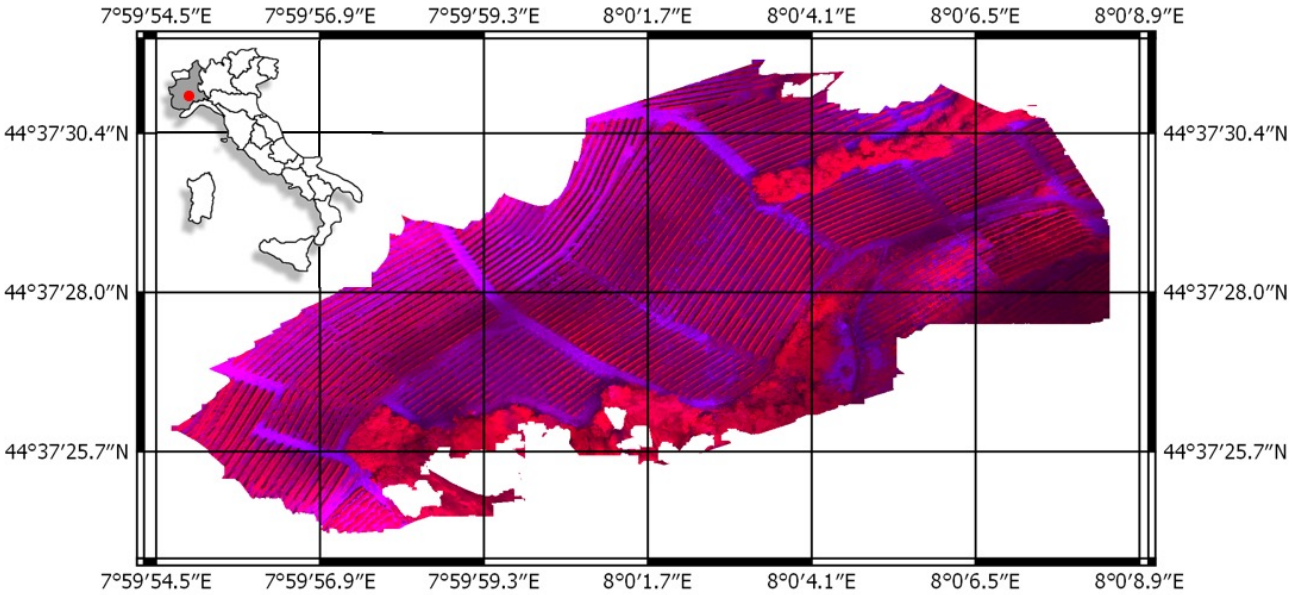

Fig. 1. False colour map (Near infrared, red, green bands) of the considered vineyard region, located in Diano d'Alba (Piedmont, Northwest of Italy).

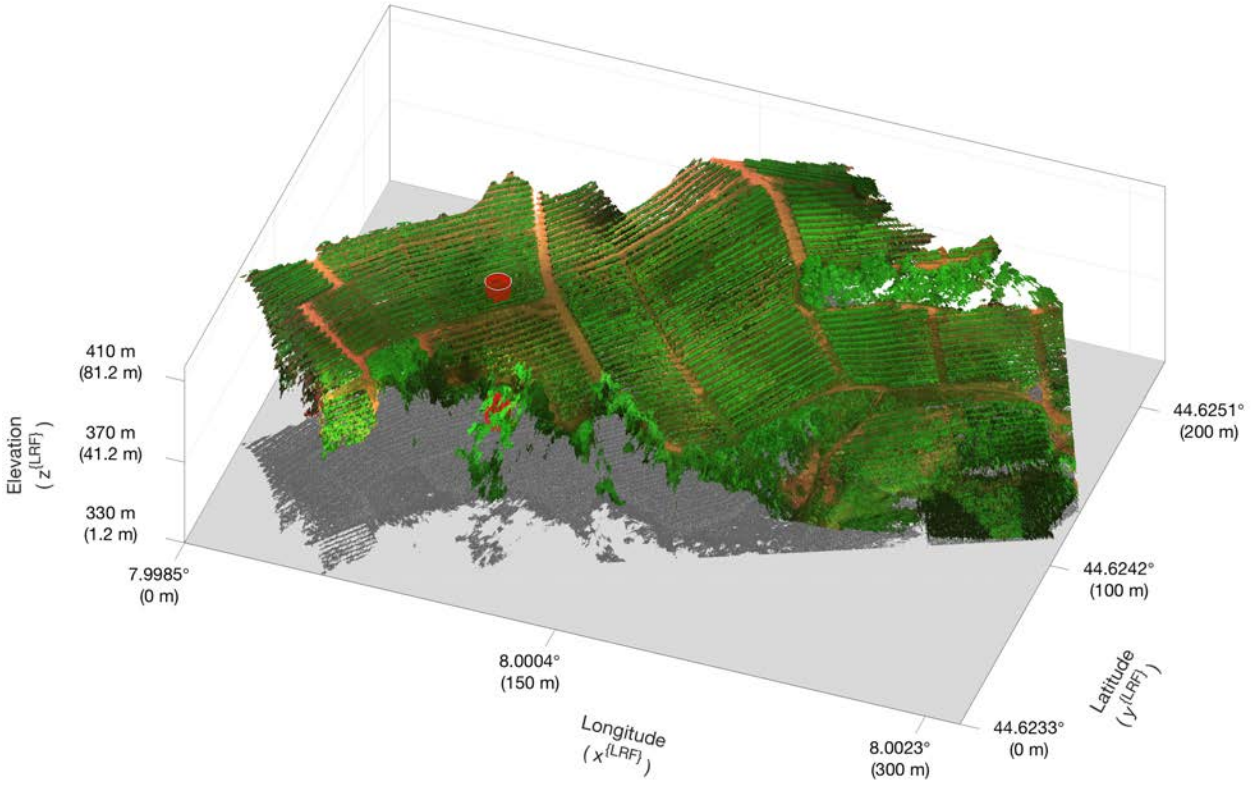

Fig. 2. Point-cloud map S_1 (June 29th 2017). The cylinder, centered in $a = (90, 110)$, out-bounding subset $\mathcal{A}_{x_a,y_a}$ is red highlighted.

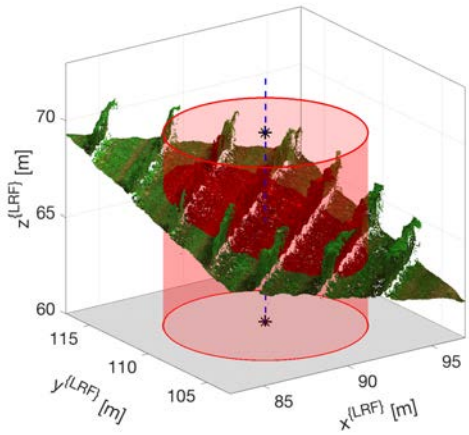

Fig. 3. Enlargement of subset $\mathcal{A}_{x_a,y_a}$, highlighted in Fig. 1, constituted of points within the cylindrical volume (red), having radius $r_{\mathcal{A}} = 5$ m and vertical axis $\mathcal{L}$ (blue dashed line) passing through $a = (90, 110)$.

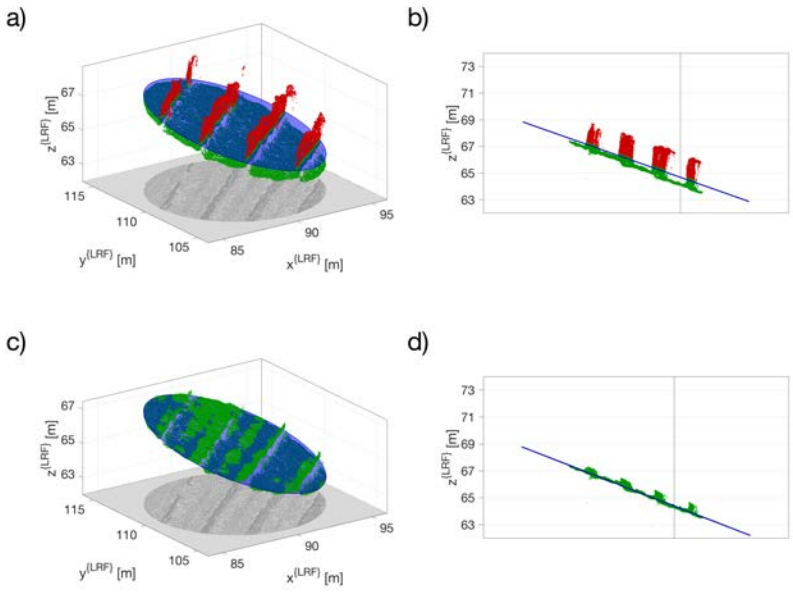

Fig. 4. Subset $\mathcal{A}_{x_a,y_a}$ (green and red points) and the interpolating plane T_0 (blue surface) are shown in perspective (a) and section (b) views. Green points form subset $\mathcal{A}^{(1)}_{x_a,y_a} \subset \mathcal{A}_{x_a,y_a}$, discarding red ones. Subset $\mathcal{A}^{(n)}_{x_a,y_a}$ (green points) and final plane $T^{(n)}$ (blue surface), modelling the local terrain surface, are shown in perspective (c) and section (d) views.

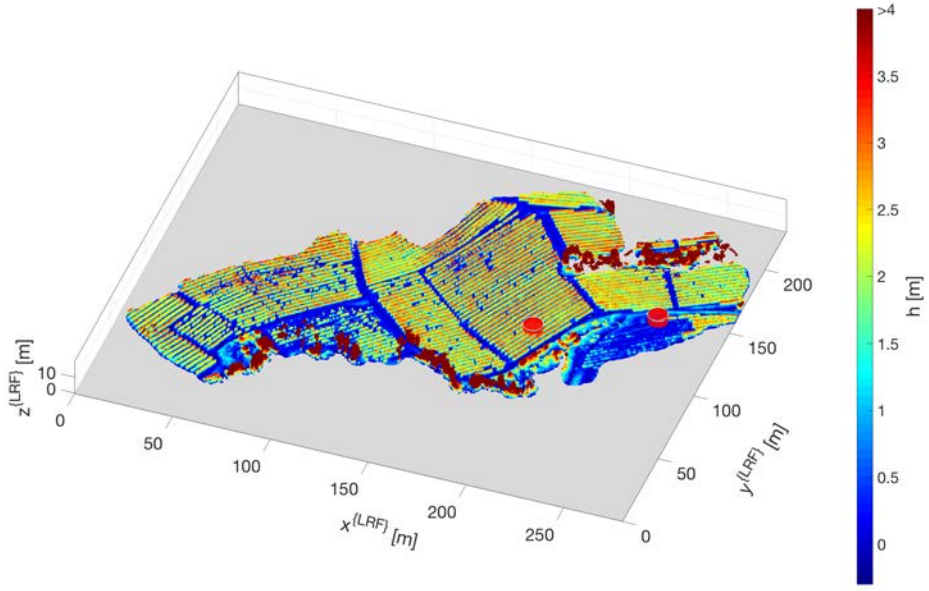

Fig. 5. Point-cloud map S_2. To enhance readability, relative height h of point $q \in S_2$ with respect to the terrain is represented by using a colour map. The two sample subsets $\mathcal{B}_{x_b,y_b}$ and $\mathcal{B}_{x_c,y_c}$, centered in $b = (200, 130)$ and $c = (230, 140)$, are marked with red cylinders.

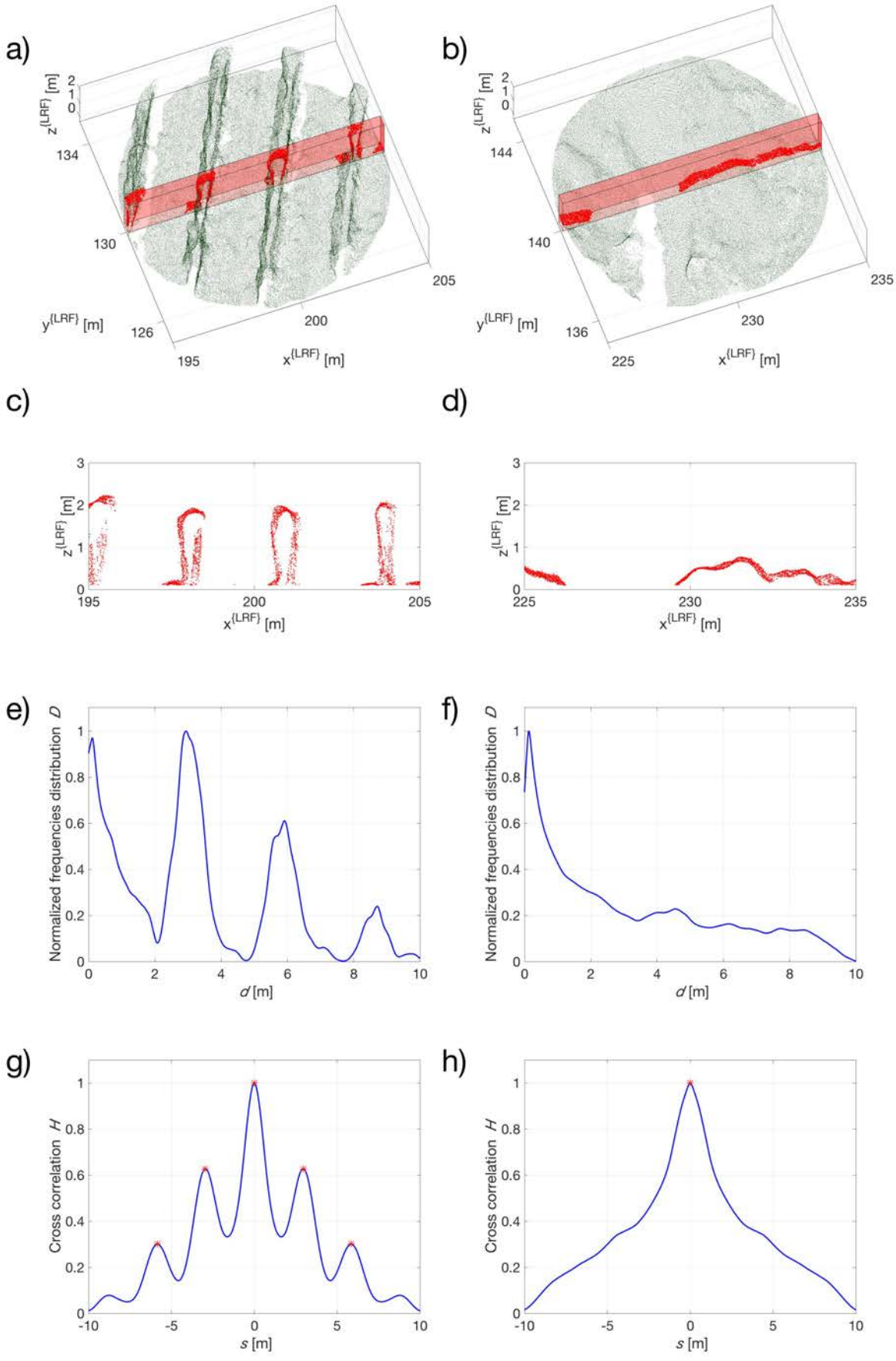

Fig. 6. Enlargements of subsets $\mathcal{B}_{x_b,y_b}$(a) and $\mathcal{B}_{x_c,y_c}$(b), centered in $b = (200, 130)$ and $c = (230, 140)$

respectively. Points belonging to subset $\mathcal{B}'_{x_b,y_b}(\vartheta)$ (c) and $\mathcal{B}'_{x_c,y_c}(\vartheta)$ (d), with $\vartheta = \pi/2$, and the between-points distances normalised frequencies distribution histogram $H\left(\mathcal{D}\left(\mathcal{B}'_{x_b,y_b}\left(\frac{\pi}{2}\right)\right), s\right)$ (e) and $H\left(\mathcal{D}\left(\mathcal{B}'_{x_c,y_c}\left(\frac{\pi}{2}\right)\right), s\right)$ (f). Finally, autocorrelation $R_{HH}(v)$ (blue solid line) of $H\left(\mathcal{D}\left(\mathcal{B}'_{x_b,y_b}\left(\frac{\pi}{2}\right)\right), s\right)$ (g) and $H\left(\mathcal{D}\left(\mathcal{B}'_{x_c,y_c}\left(\frac{\pi}{2}\right)\right), s\right)$ (h), and detected local maxima (red star markers).

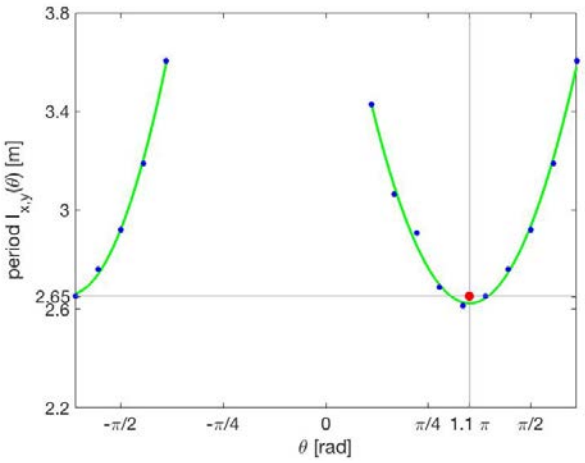

Fig. 7. Set of period values $I_{x_b,y_b}(\vartheta) \in \mathbb{I}_{x_b,y_b}$ (blue dots), with $\vartheta \in \Theta = \left\{-\frac{5}{9}\pi, -\frac{\pi}{2}, -\frac{8}{18}\pi, \ldots, \frac{5}{9}\pi\right\}$, and the second order polynomial interpolating functions $f_p(\vartheta)$ (green solid line). The score $m(x_b, y_b)$ of local subset $\mathcal{B}_{x_b,y_b}$ is 0.65, while $m(x_c, y_c)$ is equal to zero. Local vine row orientation $\vartheta_v(x_b, y_b)$ is derived from the interpolating function minimum $\vartheta_{\perp v}$, in 1.1π radiant (red point). Evaluating $I_{x,y}(\vartheta_{\perp v})$, the local inter row spacing $d_v(x_b, y_b) = 2.65$ m can be found (red point).

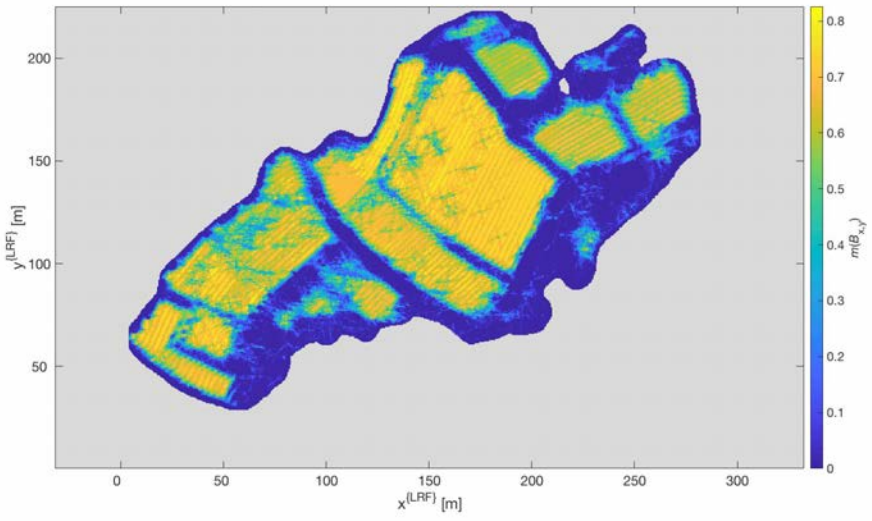

Fig. 8. Vineyard likelihood score map $M(S_2)$.

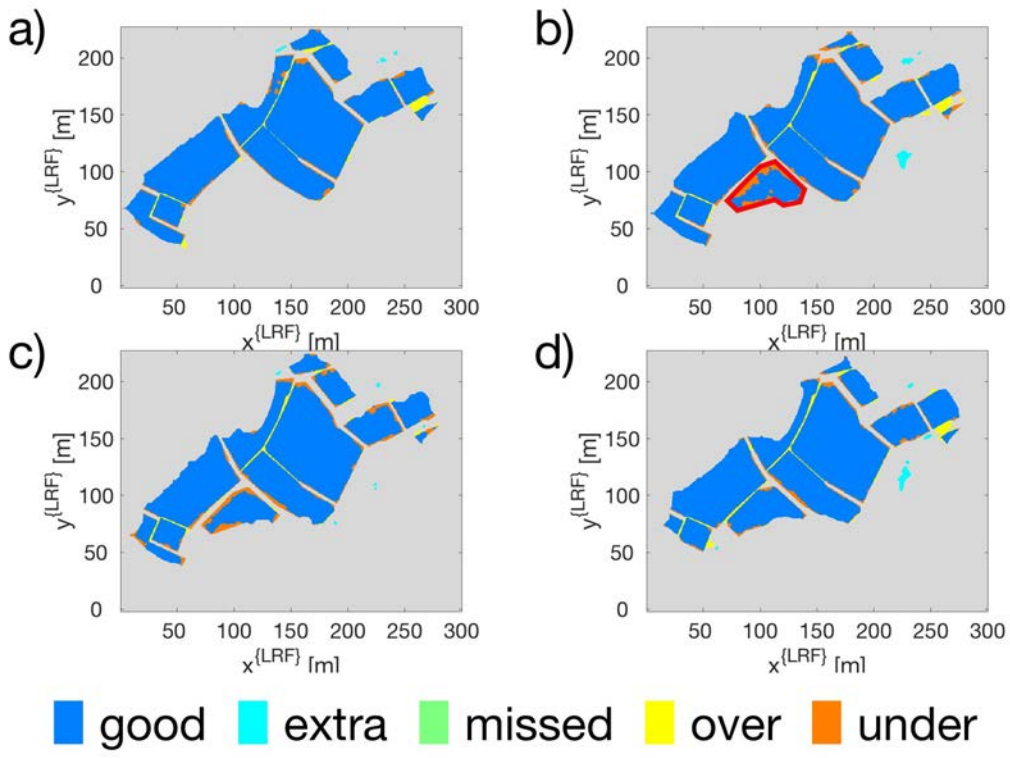

Fig. 9. Graphical representation of algorithm performances, on the base of indexes defined in Table 1, obtained processing point-cloud of May 15th 2017 (a), June 29th 2017 (b), August 1st 2017 (c) and September 23rd 2017 (d) flights. Red marked parcel (b) was planted in spring 2017.

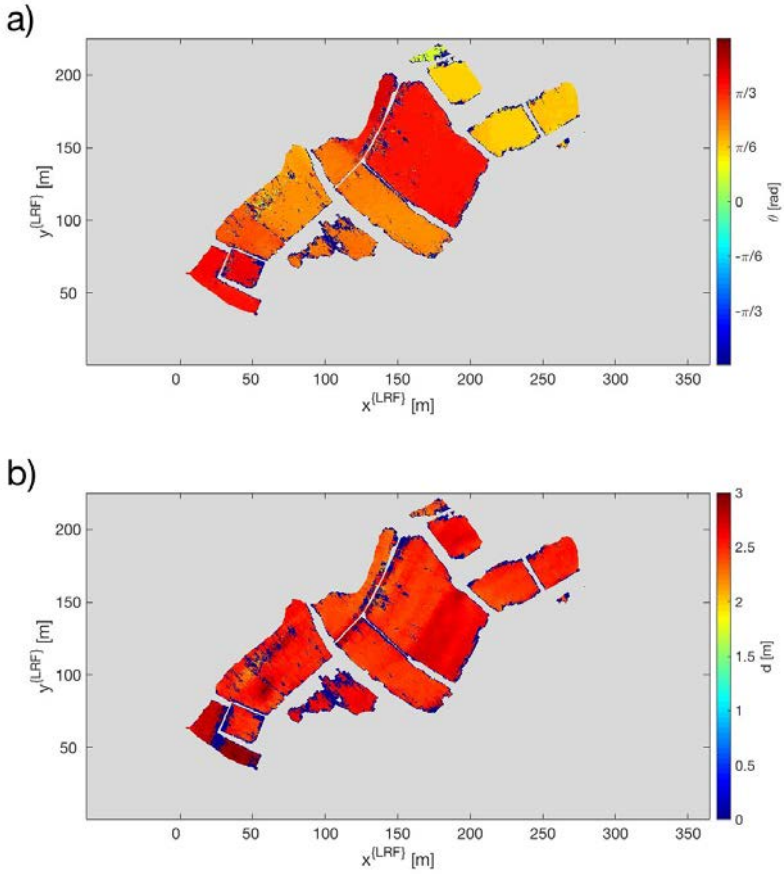

Fig. 10. Maps of local vine row direction $\vartheta_v(x, y)$ (a) and local inter row spacing $d_v(x, y)$ (b) obtained processing the point-cloud map of June 29th 2017.

Acknowledgements

This research was partially funded by project VITIFUTURE (POR FESR 2014-2020, Polo Innovazione AgriFood). The authors would like to acknowledge Germano Ettore, owner of the winery, for hosting the experimental campaign and Iway S.r.l. for conducting UAV flights and 3D point-clouds acquisitions.

Appendix A. Supplementary materials

Supplementary materials (video files) are provided online in the electronic version of the paper in Elsevier Web products, including ScienceDirect.

References

Agisoft©, 2017. http://www.agisoft.com.

Arango, R.B., Campos, A.M., Combarro, E.F., Canas, E.R., Díaz, I., 2016. Mapping cultivable land from satellite imagery with clustering algorithms. Int J Appl Earth Obs 49, 99 - 106.

Arnó, J., Martinez-Casasnovas, J.A., Ribes-Dasi, M., Rosell, J.R., 2011. Clustering of grape yield maps to delineate site-specific management zones. Span J Agric Res 9, 721 - 729.

Asproudi, A., Petrozziello, M., Cavalletto, S., Guidoni, S., 2016. Grape aroma precursors in cv. Nebbiolo as affected by vine microclimate. Food Chem 211, 947 - 956.

Blauth, D.A., Ducati, J.R., 2010. A Web-based system for vineyards management, relating inventory data, vectors and images. Comput Electron Agr 71, 182 - 188.

Cai, G., Chen, B. M., Lee, T. H. Unmanned Rotorcraft Systems, Advances in Industrial Control. © Springer-Verlag London Limited 2011.

Chang, A., Jung, J., Maeda, M.M., Landivar, J., 2017. Crop height monitoring with digital imagery from Unmanned Aerial System (UAS). Comput Electron Agr 141, 232 - 237.

Comba, L., Gay, P., Primicerio, J., Ricauda Aimonino, D., 2015. Vineyard detection from unmanned aerial systems images. Comput Electron Agr 114, 78 - 87.

Costa, J.M., Vaz, M., Escalona, J., Egipto, R., Lopes, C., Medrano, H. et al., 2016. Modern viticulture in southern Europe: Vulnerabilities and strategies for adaptation to water scarcity. Agr Water Manage 164, 5 - 18.

Da Costa, J.P., Michelet, F., Germain, C., Lavialle, O., Grenier, G., 2007. Delineation of vine parcels by segmentation of high resolution remote sensed images. Precision Agric 8, 95 - 100.

Delenne, C., Durrieu, S., Rabatel, G., Deshayesa, M., 2010. From pixel to vine parcel: a complete methodology for vineyard delineation and characterization using remote-sensing data. Comput Electron Agr 70, 78 - 83.

García-Santillán, I.D., Montalvo, M., Guerrero, J.M., Pajares, G., 2017. Automatic detection of curved and straight crop rows from images in maize fields. Biosyst Eng 156, 61 - 79.

Gimenez, J., Herrera, D., Tosetti, S., Carelli, R., 2015. Optimization methodology to fruit grove mapping in precision agriculture. Comput Electron Agr 116, 88 - 100.

Guo, H., Ma, X., Ma, Q., Wang, K., Su, W., Zhu, D., 2017. LSSA_CAU: An interactive 3d point clouds analysis software for body measurement of livestock with similar forms of cows or pigs. Comput Electron Agr 138, 60 - 68.

Haase, M., Rösch, C., Ketzer, D., 2016. GIS-based assessment of sustainable crop residue potentials in European regions. Biomass Bioenerg 86, 156 - 171.

Hall, A., Lamb, D.W., Holzapfel, B.P., Louis, J.P., 2011. Within-season temporal variation in correlations between vineyard canopy and winegrape composition and yield. Precis Agric 12, 103 - 177.

Herrero-Huerta, M., González-Aguilera, D., Rodriguez-Gonzalvez, P., Hernández-López, D., 2015. Vineyard yield estimation by automatic 3D bunch modelling in field conditions. Comput Electron Agr 110, 17 - 26.

Khanal, S., Fulton, J., Shearer, S., 2017. An overview of current and potential applications of thermal remote sensing in precision agriculture. Comput Electron Agr 139, 22 - 32.

Lipiński, A.J., Markowski, P., Lipiński, S., Pyra, P., 2016. Precision of tractor operations with soil cultivation implements using manual and automatic steering modes. Biosyst Eng 145, 22 - 28.

MacDonald, S.L., Staid, M., Staid, M., Cooper, M.L., 2016. Remote hyperspectral imaging of grapevine leafroll-associated virus 3 in cabernet sauvignon vineyards. Comput Electron Agr 130, 109 - 117.

Mack, J., Lenz, C., Teutrine, J., Steinhage, V., 2017. High-precision 3D detection and reconstruction of grapes from laser range data for efficient phenotyping based on supervised learning. Comput Electron Agr 135, 300 - 311.

Malambo, L., Popescu, S.C., Murray, S.C., Putman, E., Pugh, N.A., Horne, D.W., et al., 2018. Multitemporal field-based plant height estimation using 3D point clouds generated from small unmanned aerial systems high-resolution imagery. Int J Appl Earth Obs 64, 31 - 42.

Mania, E., Isocrono, D., Pedullà, M. L., Guidoni, S., 2015. Plant Diversity in an Intensively Cultivated Vineyard Agroecosystem (Langhe, North-West Italy). S Afr J Enol Vitic 36, 378 - 388.

Mathworks Matlab®, 2018. https://www.mathworks.com/products/matlab.html.

Mortensen, A.K., Lisouski, P., Ahrendt, P., 2016. Weight prediction of broiler chickens using 3D computer vision. Comput Electron Agr 123, 319 - 326.

Parrot© SA, 2017. https://www.parrot.com/global/business-solutions/parrot-sequoia.

Primicerio, J., Caruso, G., Comba, L., Crisci, A., Gay, P., Guidoni, S., et al., 2017. Individual plant definition and missing plant characterization in vineyards from high-resolution UAV imagery. Eur J Remote Sens 50, 179 - 186.

Primicerio, J., Gay, P., Ricauda Aimonino, D., Comba, L., Matese, A., Di Gennaro, S. F., 2015. NDVI based vigour maps production using automatic detection of vine rows in ultra-high resolution aerial images. European Conference (10th) on Precision Agriculture, 465 - 470.

QGIS, 2018. https://www.qgis.org/en/site/.

Quebrajo, L., Perez-Ruiz, M., Pérez-Urrestarazu, L., Martínez, G., Egea, G., 2018. Linking thermal imaging and soil remote sensing to enhance irrigation management of sugar beet. Biosyst Eng, 165, 77-87.

Rabatel, G., Delenne, C., Deshayes, M., 2008. A non-supervised approach using Gabor filters for vine-plot detection in aerial images. Comput Electron Agr 62, 159 - 168.

Reina, G., Milella, A., Galati, R., 2017. Terrain assessment for precision agriculture using vehicle dynamic modelling. Biosyst Eng 162, 124 - 139.

Rodrigo Comino, J., Senciales, J.M., Ramos, M.C., Martínez-Casasnovas, J.A., Lasanta, T., Brevik, E.C., Ries, J.B., Ruiz Sinoga, J.D., 2017. Understanding soil erosion processes in Mediterranean sloping vineyards (Montes de Málaga, Spain). Geoderma 296, 47 - 59.

Sankey, T., Donager, J., McVay, J., Sankey, J.B., 2017. UAV lidar and hyperspectral fusion for forest monitoring in the southwestern USA. Remote Sens Environ 195, 30 - 43.

Shah, S.A.A., Bennamoun, M., Boussaid, F., 2017. Keypoints-based surface representation for 3D modeling and 3D object recognition. Pattern Recogn 64, 29 - 38.

Stojanovic, V., Falconer, R.E., Isaacs, J., Blackwood, D., Gilmour, D., Kiezebrink, D., Wilson, J., 2017. Streaming and 3D mapping of AGRI-data on mobile devices. Comput Electron Agr 138, 188 - 199.

Sture, Ø., Øye, E.R., Skavhaug, A., Mathiassen, J.R., 2016. A 3D machine vision system for quality grading of Atlantic salmon. Comput Electron Agr 123, 142 - 148.

Su, Q., Kondo, N., Li, M., Sun, H., Al Riza, D.F., 2017. Potato feature prediction based on machine vision and 3D model rebuilding. Comput Electron Agr 137, 41 - 51.

Torres-Sánchez, J., Peña, J.M., de Castro, A.I., López-Granados, F., 2014. Multi-temporal mapping of the vegetation fraction in early-season wheat fields using images from UAV. Comput Electron Agr 103, 104 - 113.

Urretavizcaya, I., Santesteban, L.G., Tisseyre, B., Guillaume, S., Miranda, C., Royo, J.B., 2014. Oenological significance of vineyard management zones delineated using early grape sampling. Precis Agric 15, 111 - 129.

Zarco-Tejada, P.J., Guillén-Climent, M.L., Hernández-Clemente, R., Catalina, A., González, M.R., Martín, P., 2013. Estimating leaf carotenoid content in vineyards using high resolution hyperspectral imagery acquired from an unmanned aerial vehicle (UAV). Agr Forest Meteorol 171-172, 281 - 294.

Zhang, C., Kovacs, J.M., 2012. The application of a small unmanned aerial systems for precision agriculture: a review. Precision Agric 13, 693 - 712.